Chapter 5 Layer/ Morphology/ Substrate Dependence on Thermal Transport Properties of MoS_2

5.1 Introduction

Two-dimensional (2D) molybdenum disulfide (MoS_2) has aroused scientific breakthrough in technologies, particularly in next-generation photonics, nanoelectronics and optoelectronic applications [8, 169-172], owing to its tunable bandgap of ~1.8 eV for monolayer to ~1.29 eV for bulk, large mobility (theoretical values around 410 $cm^2V^{-1}s^{-1}$ and experimental values ranging from 0.1 to 10 $cm^2V^{-1}s^{-1}$) and a high current on/off ratios of 10^{10} [33, 75, 76]. The utilization of these materials in device fabrication requires the knowledge of their thermal, electrical and optical properties and are indeed strongly influenced by the interaction of electrons and phonons [173, 174]. At high current density, excess self-heating is produced in the device due to applied bias and the back gate voltage, causing highly localized Joule heating that creates hot spots. Thereafter, more phonons get excited and electron-phonon scattering rate increases, that declines the carrier mobility and obstructs the electron transport properties. Thus, for device application, there is an increasing demand for more effective heat management to minimise the self-heating. Also, the fabrication of MoS_2 based devices requires the support or transfer of MoS_2 onto a substrate and this supporting substrate also affects the thermal properties of device as maximum heat dissipation occurs from the out-of-plane direction (interfacial thermal conductance). Hence, understanding the thermal properties like thermal conductivity and interfacial thermal conductance between the grown MoS_2 film and the substrate are imperative to fabricate integrated electronic and optoelectronic devices at large-scale. Another requirement for the application of MoS_2 in various integrated circuits requires the growth of large-area, high quality and continuous film of MoS_2 over the supportive substrate. Among the various methods available, as discussed in **Chapter 2**, the scalable synthesis via chemical vapor deposition (CVD) technique offers considerable interests.

There are different thermal transport techniques, such as time domain differential Raman technique, variable-spot size laser-flash Raman method, two-laser Raman thermometry, etc., to measure the interfacial thermal conductance and thermal conductivity of layered MoS_2, as already discussed in **Chapter 1**. Both theoretical and experimental techniques have been investigated previously to obtain the thermal conductivity of MoS_2 [47, 175, 176]. Theoretical evaluation of thermal conductivity of MoS_2 was mostly performed on monolayer [177, 178]. Theoretical simulation using PBTE calculations predicted the decrease in thermal conductivity for suspended MoS_2 with increasing thickness from single to three layers [177]. Thermal conductivity (k_s) in the range 44 to 52 W m^{-1} K^{-1} was obtained for suspended few layers (4-7 layers) exfoliated MoS_2 using thermal bridge method [65]. The nanosecond ET-Raman technique shows k_s varying from 40 to 74 W m^{-1} K^{-1} for exfoliated MoS_2, as thickness increases from 45 to 115 nm [176]. Among different thermal transport techniques, the optothermal Raman technique is a straightforward and non-destructive technique to measure the interfacial thermal conductance and thermal conductivity of layered MoS_2 [179]. In this method, excitation source is focussed on the surface of the sample, serving both as a heat source and a temperature probe. The schematic setup for the optothermal Raman study is shown in **Figure 5.1**. There are only few studies on thermal transport measurement of supported MoS_2 nanostructures using optothermal Raman technique, as described in **Chapter 1.** Most of the reports on thermal conductivity evaluation of MoS_2 is based on mechanically exfoliated (suspended/supported) samples. However, the studies on CVD grown supported MoS_2 nanostructures with varying thickness and on thin film CVD grown MoS_2 supported over conducting substrate are still missing in the literature. Moreover, the comprehensive reports invoking the anharmonic (non-linearity) temperature-dependent phonon response of CVD grown supported MoS_2 are still lacking.

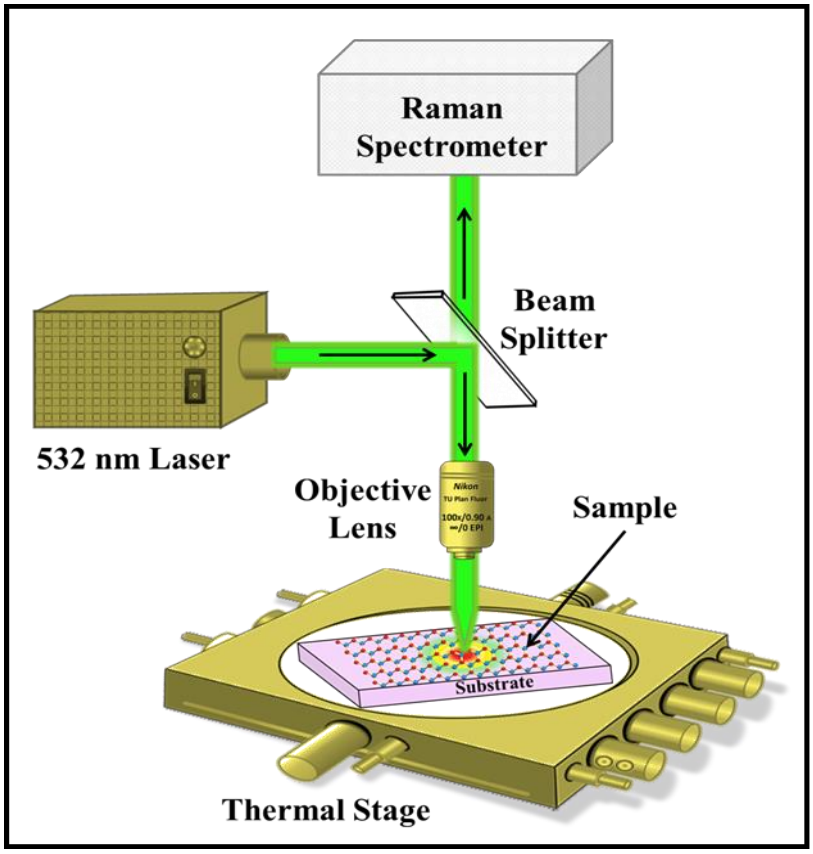

Figure 5.1 *Schematic showing the setup for optothermal Raman study.*

In the present chapter, we have studied the thermal sensitive phonon confinement behavior of 1L, 3L and 5L triangular MoS_2, H-MoS_2/SiO_2-Si, V-MoS_2/SiO_2-Si and H-MoS_2/FTO in the low-temperature regime 80 K to 300 K, to understand their linear and non-linear thermal response. We have also estimated the interfacial thermal conductance per unit area (g) and thermal conductivity (k_s) of as-synthesized samples using optothermal Raman technique.

5.2 Results and Discussion

5.2.1 Higher Order Phonon Scattering and Thermal Transport Properties of 1L, 3L and 5L Triangular MoS_2/SiO_2-Si

In this section, we have performed the thermal analysis of phonon confinement by examining the temperature-dependent phonon evolution of different layered (1L, 3L and 5L) triangular MoS_2 nanostructures grown over SiO_2-Si substrate**.** We have quantitatively analyzed

the non-linear temperature-dependent Raman shift by employing a physical model that incorporates thermal expansion, three- and four-phonon anharmonic effects. We have also measured the interfacial thermal conductance (g) and thermal conductivity (k_s) of 1L, 3L and 5L triangular MoS_2 supported on SiO_2-Si substrate using combined temperature and power-dependent Raman studies.

5.2.1.1 Characterization of 1L, 3L and 5L Triangular MoS_2/SiO_2-Si

The optical image of CVD grown different layered (1L, 3L and 5L) triangular MoS_2 grown over SiO_2-Si substrate is shown in **Figure 2.5 (a)** of **chapter 2**, indicating 5-15 μm lateral dimensions of each triangle of MoS_2. The Raman spectrum of these 1L, 3L and 5L triangular MoS_2 are shown in **Figure 2.13 (a)** of **chapter 2**. The presence of two characteristic peak (in-plane E^1_{2g} and out-of-plane A_{1g}) confirms the 2H phase of MoS_2. The frequency difference between these two peaks suggests the growth of 1L, 3L and 5L MoS_2 and is consistent with previous reports [123, 124]. The corresponding PL spectra of synthesized 1L, 3L and 5L triangular MoS_2 are shown in **Figure 2.15 (a)** of **chapter 2**. Two major PL peaks at ~1.85 eV (A-exciton) and 1.98 eV (B-exciton) are observed and are attributed to the direct bandgap transition at K-point. The AFM image and corresponding height profile of 1L, 3L and 5L triangular MoS_2/SiO_2-Si are shown in **Figure 2.10 (a-c)** of **chapter 2**.

5.2.1.2 Temperature-Dependent Raman Study of 1L, 3L and 5L Triangular MoS_2/SiO_2-Si

We perform the temperature-dependent Raman study using 50x LWD lens in the temperature range 80 to 300 K. The temperature-dependent Raman spectra (Lorentzian fitted) of 1L, 3L and 5L triangular MoS_2/SiO_2-Si in the temperature range of 80 to 193 K and 213 to 333 K are shown in **Figure 5.2**. The layer dependent frequency shift of both the phonon modes is attributed to weak van der Waals interlayer interaction. At lower temperature, the phonon

shifts of both the modes (E^1_{2g} and A_{1g}) are observed to be relatively slow and as the temperature increases ($k_BT >> \hbar\omega$), this shift increases and exhibits to soften linearly with temperature.

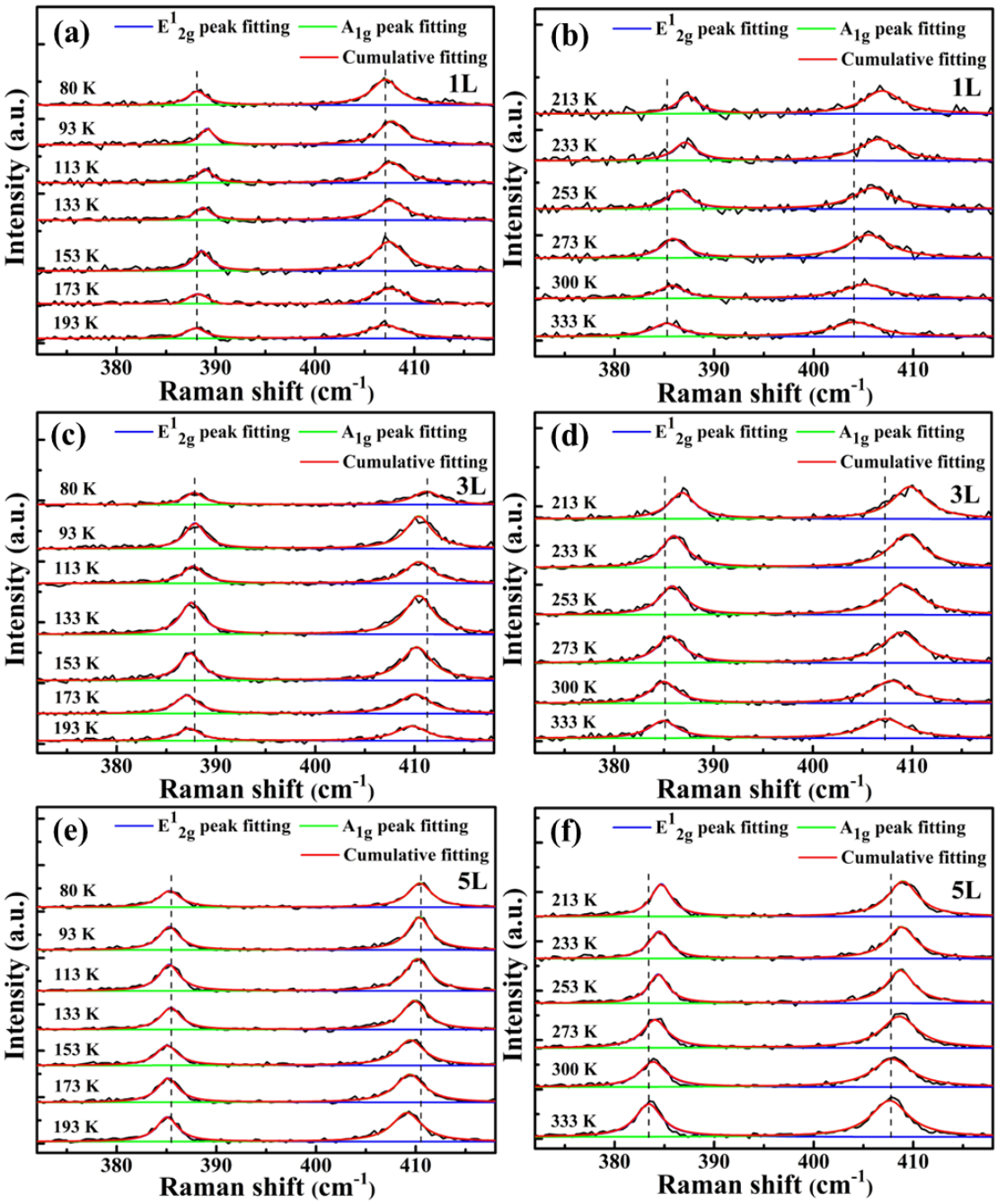

Figure 5.2 *Temperature-dependent phonon response from 80 to 193 K and from 213 to 333 K of (a, b) 1L, (c, d) 3L and (e, f) 5L CVD grown triangular MoS_2/SiO_2-Si using 50x LWD lens.*

Firstly, we analyse the temperature-dependent Raman shift of E^1_{2g} and A_{1g} phonon modes by a linear approximation given by Grüneisen model [180]-

$$\omega\,(T) = \omega_0 + \chi_T T \qquad (5.1)$$

where ω_0 is the extrapolated peak position of E^1_{2g} and A_{1g} modes at 0 K and the slope χ_T is the first order temperature coefficient, showing the frequency shift of the respective phonon mode when temperature is raised by 1K. The best linear fitting of 1L, 3L and 5L MoS_2 for both the phonon modes is plotted in **Figure 5.3 (a)**. The extracted χ_T values of E^1_{2g} (A_{1g}) mode are 0.0179 (0.0112), 0.0143 (0.0163) and 0.0066 (0.0113) cm^{-1} K^{-1} for 1L, 3L and 5L MoS_2, respectively. Since E^1_{2g} mode exhibits a larger frequency shift than A_{1g} for 1L MoS_2 and hence its thermal transport behavior is examined by E^1_{2g} mode. The A_{1g} mode becomes more effective with the increase in the layer number, hence thermal transport behavior of the different layered (3L and 5L) MoS_2 film is usually examined by A_{1g} mode. The variation of FWHM of both the phonon modes of prepared MoS_2 with temperature is given in **Figure 5.3 (b)**. The FWHM of each mode increases linearly with increasing temperature, indicating the softening of bonds with temperature. Some degree of deviation from linearity has also been observed in phonon shifts, suggesting possible anharmonicity in prepared MoS_2 film.

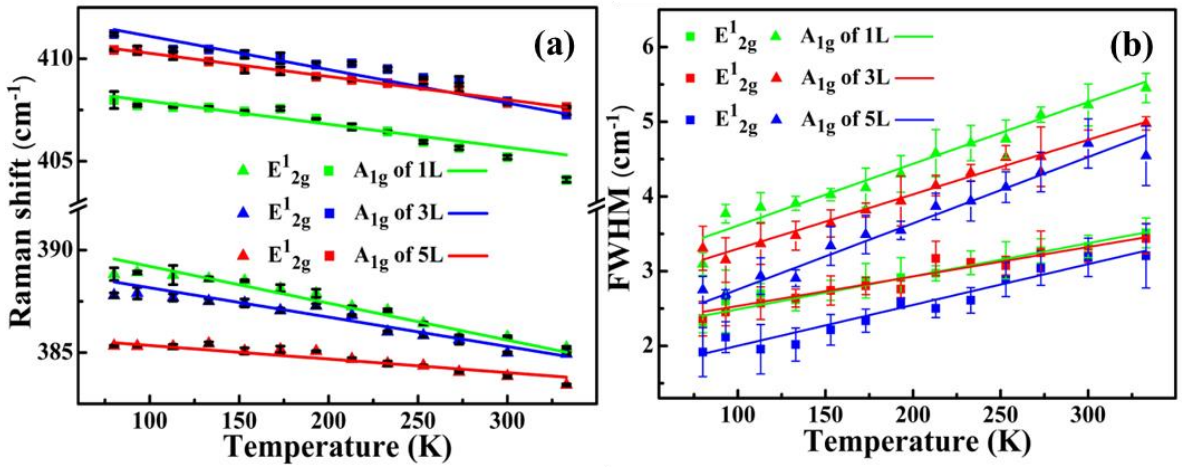

Figure 5.3 *Variations of (a) peak position and (b) FWHM of E^1_{2g} and A_{1g} modes with temperature for 1L, 3L and 5L triangular MoS_2.*

To analyse the origin of nonlinearity in temperature-dependent response of E^1_{2g} and A_{1g} modes, a semiquantitative model is used that takes into account the contributions from pure volume effect and pure temperature effect. The pure volume effect arises from the thermal expansion of the lattice $(\Delta\omega)_{latt}$ and the pure temperature effect is due to anharmonic phonon-

phonon interaction $(\Delta\omega)_{anh}$ which arises from the cubic and quartic anharmonicities (self-energy shift). The cubic and quartic anharmonicities includes contributions from three- and four-phonon anharmonic process. Hence within this model, the overall frequency shift with temperature can be expressed as -

$$\omega(T) = \omega_0 + (\Delta\omega)_{latt} + (\Delta\omega)_{anh} \quad (5.2)$$

Thermal expansion contribution is described by the Grüneisen constant model as follows [181]-

$$\Delta\omega_{latt} = \omega_0 \{\exp\left(-n\gamma \int_0^T \alpha_T dT\right) - 1\} \quad (5.3)$$

where n is the degeneracy with the value of 1 for A_{1g} mode and 2 for E^1_{2g} mode, γ is the Grüneisen parameter and α_T is the thermal expansion coefficient. The integral in the above equation depicts the diminution of the vibration frequency caused by the volume expansion. The Grüneisen parameter depends on the restoring force between atoms and varies weakly with the layer number of the material. Thus, for simplicity, we assume constant value of Grüneisen parameter for different layered MoS_2, i.e. γ (E^1_{2g}) = 0.21 and γ (A_{1g}) = 0.42 [33]. Thermal expansion coefficient for both modes have been derived by El-Mahalawy and Evans as [33]-

$$\alpha_a = \frac{(0.6007\times10^{-5} + 0.6958\times10^{-7}T)}{a}\left(\frac{1}{℃}\right) \quad (5.4)$$

$$\alpha_c = \frac{(0.1064\times10^{-3} + 1.5475\times10^{-7}T)}{c}\left(\frac{1}{℃}\right) \quad (5.5)$$

where T is the temperature in °C, a and c are the lattice constants of MoS_2 having values 3.127 and 12.066 Å, respectively. At room temperature, the in-plane and out-of-plane thermal expansion coefficients calculated are 2.48 × 10^{-6} °C^{-1} and 9.14 × 10^{-6} °C^{-1}, respectively. Numerous light scattering phenomena includes absorption and emission of photons along with scattering of optical phonons that decay into two or three phonons because of anharmonic interactions. The production of two- and three- phonons are individually called as three-phonon and four-phonon process, and can be simply expressed using semi-quantitative model developed by Kelmens as [181]-

$$\Delta\omega_{anh}(T) = A\left(1 + \frac{2}{e^{x}-1}\right) + B\left(1 + \frac{3}{e^{y}-1} + \frac{3}{(e^{y}-1)^{2}}\right) = \Delta\omega_{A-3p}(T) + \Delta\omega_{A-4p}(T) \quad (5.6)$$

where $x = \frac{\hbar\omega_0}{2k_B T}$ and $y = \frac{\hbar\omega_0}{3k_B T}$, k_B is the Boltzmann constant and T is the temperature in K. The coefficient A and B are the constants that represents the contribution of three- and four-phonon processes to the frequency shift, respectively and are obtained by best fitting the contributions to the experimental results. **Equations 5.2, 5.3 and 5.6** are then exploited to fit the non-linear temperature dependence of Raman shifts. The overall model, as described in **equation 5.2**, shows a better fit to the temperature-dependent non-linear Raman shift. The individual contributions of thermal expansion, three- and four-phonon process to the temperature-dependent non-linear profile of E^1_{2g} and A_{1g} modes along with the experimental data for 1L, 3L and 5L MoS_2 are plotted in **Figure 5.4 (a-f)** and corresponding fitting parameters A and B extracted for E^1_{2g} and A_{1g} modes are listed in **Table 5.1**. Three-phonon scattering (blue solid line) rules over the four-phonon scattering (pink solid line) and thermal expansion contribution (green solid line) for both the Raman modes. As the number of layer increases, both three- and four-phonon scattering decreases. As far as thermal expansion contribution is concerned, in case of E^1_{2g} mode of monolayer, the difference of thermal expansion coefficient between the substrate (SiO_2-Si) and MoS_2 film produces compressive strain in the film that effectively decreases the thermal expansion of the lattice. However, with increasing layer number the effect of compressive strain reduces and thermal expansion contribution remains nearly constant for 3L and 5L MoS_2. The thermal expansion contribution for A_{1g} mode is independent of layer number because the compressive strain effect is mainly in-plane vibration rather than out-of-plane one. Thus, this study suggests that phonon anharmonicity dominates over thermal expansion in MoS_2, which is in accord to the previous report on strong covalent materials [182].

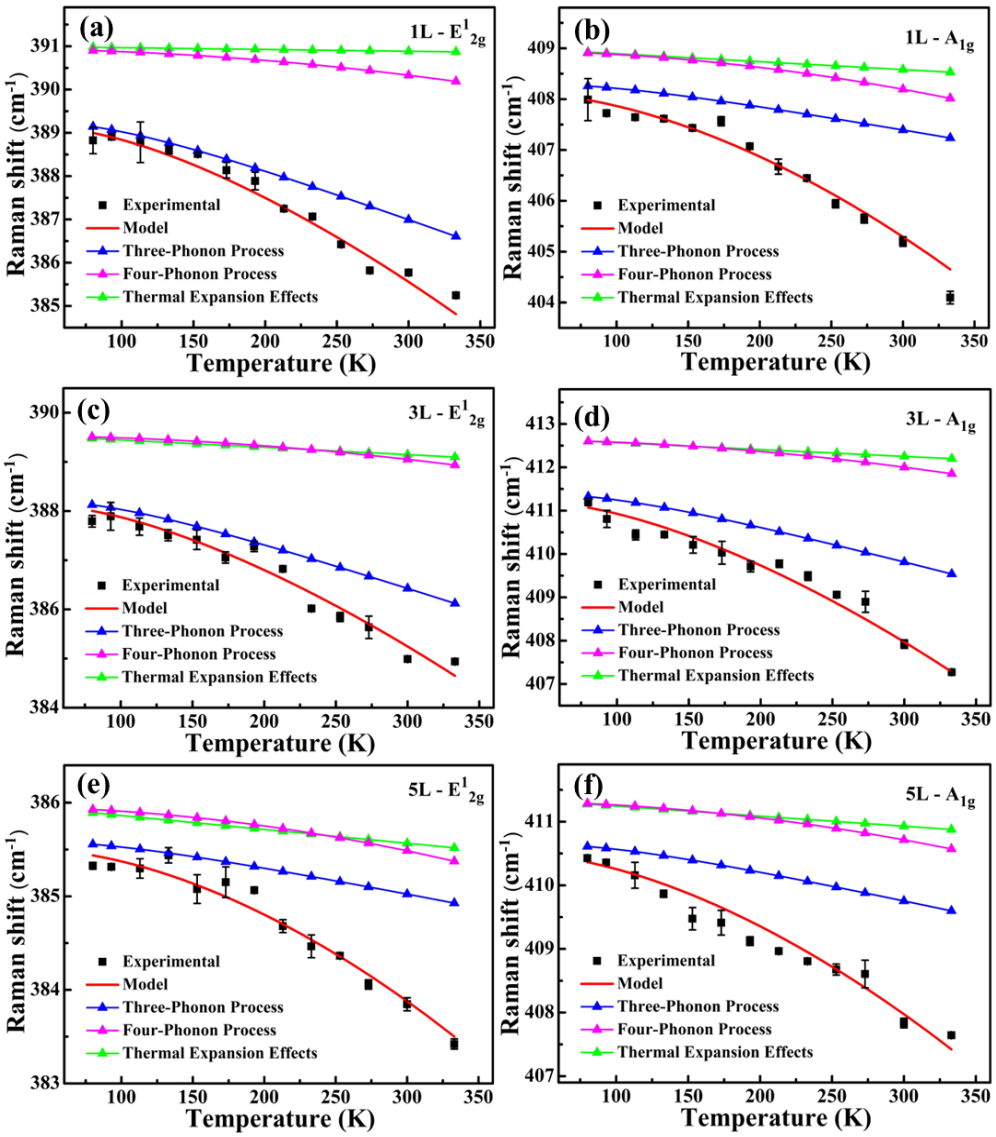

Figure 5.4 *The modelling of temperature-dependent Raman shift (red solid line) and individual theoretical contributions to experimental results (black square) from pure thermal expansion (green solid line), three-phonon (blue solid line) and four-phonon (pink solid line) of* E^1_{2g} *and* A_{1g} *modes of (a, b) 1L, (c, d) 3L and (e, f) 5L triangular* MoS_2/SiO_2*-Si.*

Table 5.1 The fitting parameters A and B for E^1_{2g} and A_{1g} phonon mode in three- and four-phonon scattering process.

Layer no.	Raman modes	W_0 (cm^{-1})	A (cm^{-1})	B (cm^{-1})
1L	E^1_{2g}	391.01	-1.76 ± 0.14	-0.08 ± 0.02
	A_{1g}	409.44	-1.01 ± 0.08	-0.11 ± 0.02
3L	E^1_{2g}	389.60	-1.38 ± 0.14	-0.06 ± 0.02
	A_{1g}	412.15	-0.94 ± 0.10	-0.10 ± 0.02
5L	E^1_{2g}	386.01	-0.43 ± 0.05	-0.06 ± 0.01
	A_{1g}	411.32	-0.86 ± 0.08	-0.07 ± 0.01

5.2.1.3 Calculation for Thermal Conductivity of 1L, 3L and 5L Triangular MoS_2/SiO_2-Si

Next, to estimate the thermal conductivity and interfacial thermal conductance of supported 1L, 3L and 5L CVD grown MoS_2 nanostructures over SiO_2-Si substrate, we inspect the phonon response with respect to local temperature rise by heating with different laser powers. In this technique, laser is focussed at the respective MoS_2 and strong thermal effects, induced by the different excitation laser power have been examined. The Lorentzian-fitted Raman spectra as a function of incident laser power using 50x LWD objective lens for 1L, 3L and 5L MoS_2 are shown in **Figure 5.5 (a-c)**. The linear peak shift in power-dependent Raman spectra is described by -

$$\omega(P) = \omega_0 + \chi_P P \tag{5.7}$$

Where P is incident laser power at the surface of the sample and first-order power-dependent coefficient, $\chi_P = \delta\omega/\delta P$, is the slope of the linear fitting of power-dependent Raman spectra (**Figure 5.5 (d)**). **Figure 5.6** shows the increase in the FWHM of both the Raman active modes with incident laser power using 50x LWD objective lens. This increase is attributed to the local rise in temperature because of laser power heating. This observation along with the redshift of both the Raman active modes with incident laser power confirms its association with the lattice expansion and softening of bonds.

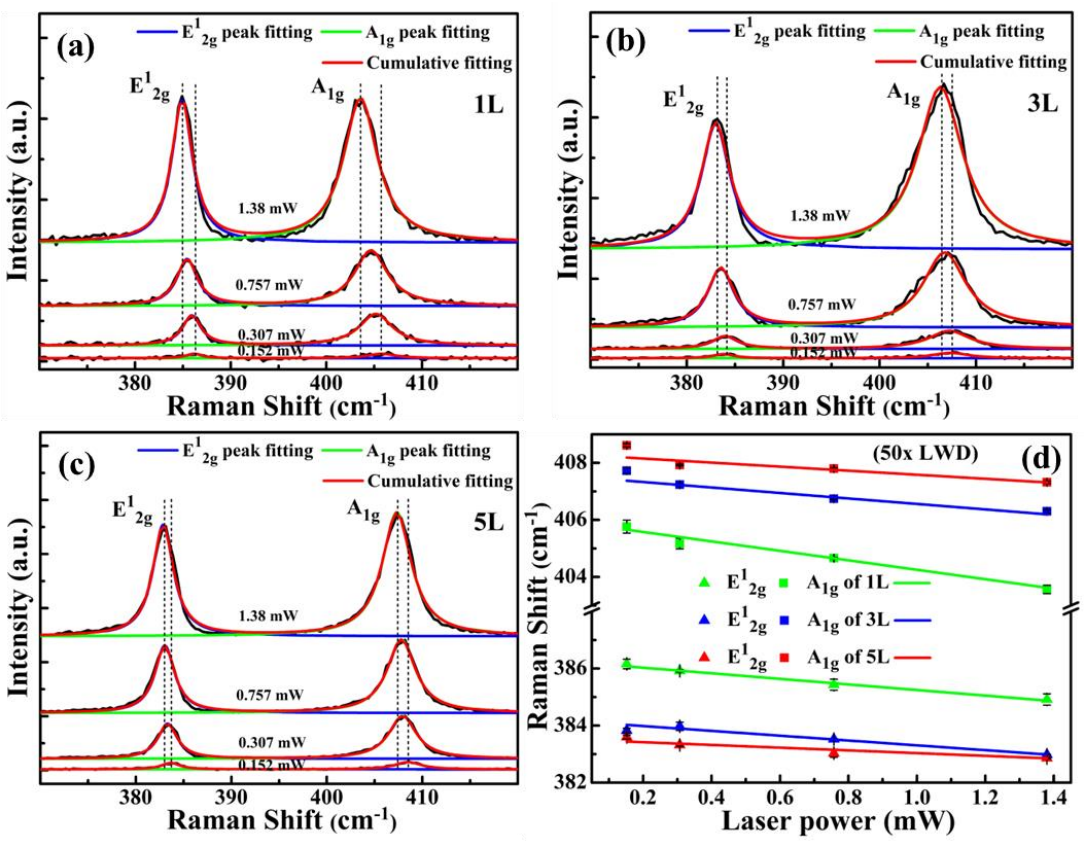

Figure 5.5 *Power-dependent Raman spectra of (a) 1L, (b) 3L and (c) 5L triangular MoS_2/SiO_2-Si using 50x LWD objective lens. (d) Variations of peak positions with incident laser power of E^1_{2g} and A_{1g} modes for 1L, 3L and 5L MoS_2.*

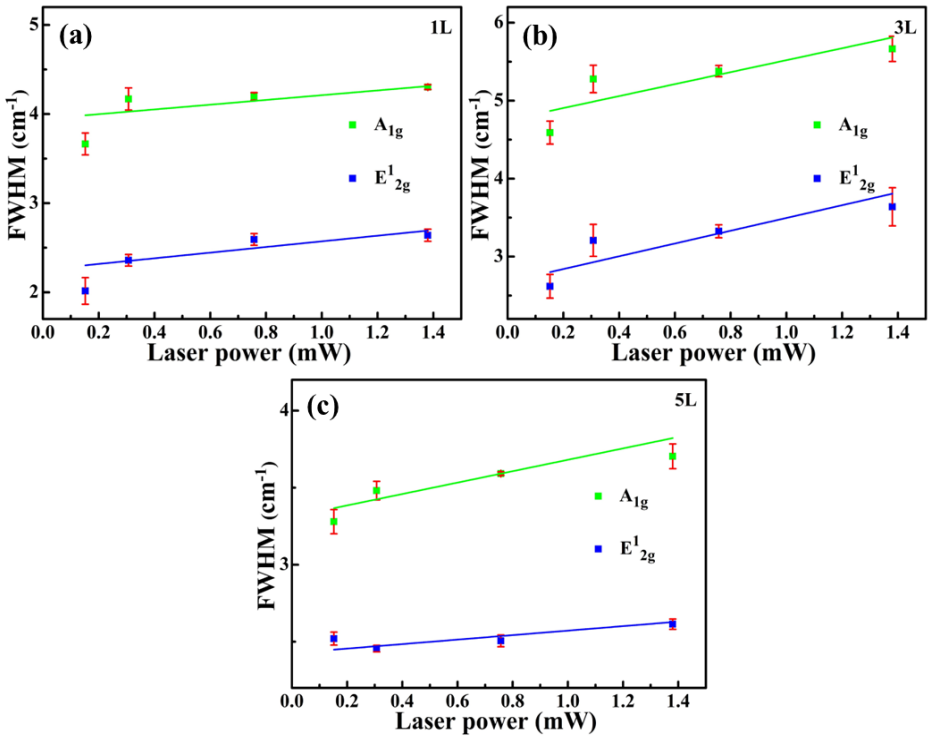

Figure 5.6 *Variations of FWHM of E^1_{2g} and A_{1g} phonon modes with incident laser power for triangular CVD grown (a) 1L, (b) 3L and (c) 5L MoS_2 using 50x LWD lens.*

Similar power-dependent Raman measurements have been performed on 1L, 3L and 5L triangular MoS_2 using 100x objective lens, as shown in **Figure 5.7 (a-c)**. The linear fittings of power-dependent Raman spectra (using **equation 5.7**), obtained using 100x objective lens, are shown in **Figure 5.7 (d)**. The χ_P values extracted for E^1_{2g} and A_{1g} phonon modes with 50x LWD and 100x objective lens are provided in **Table 5.2**. The E^1_{2g} phonon mode is observed to be lesser red shifted due to the stiffing of the E^1_{2g} phonon mode towards the laser power because of thermally induced compressive strain by substrate [183]. The laser induced thermal red shift of the two phonon modes is observed to decrease with increasing layer number.

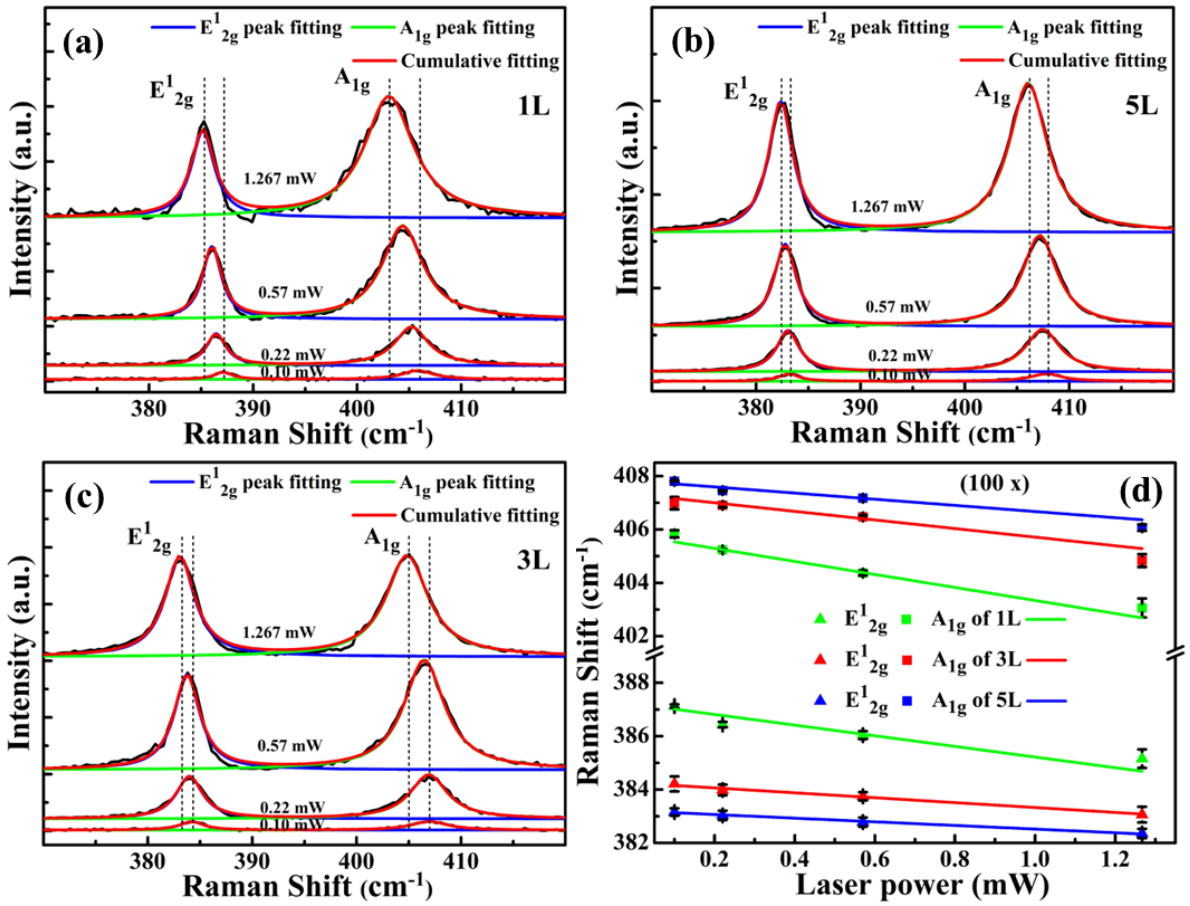

Figure 5.7 *Power-dependent Raman spectra of (a) 1L, (b) 3L and (c) 5L triangular MoS_2/SiO_2-Si using 100x objective lens. (d) Variations of peak positions with incident laser power of E^1_{2g} and A_{1g} modes for 1L, 3L and 5L MoS_2/SiO_2-Si.*

Figure 5.8 shows the increase in the FWHM of both the Raman active modes with incident laser power using 100x objective lens. The observed broadening is linked to localized

temperature elevation induced by laser heating. This phenomenon, coupled with the redshift of both the Raman active modes as the incident laser power increases, substantiates its correlation with lattice expansion and the relaxation of bonds.

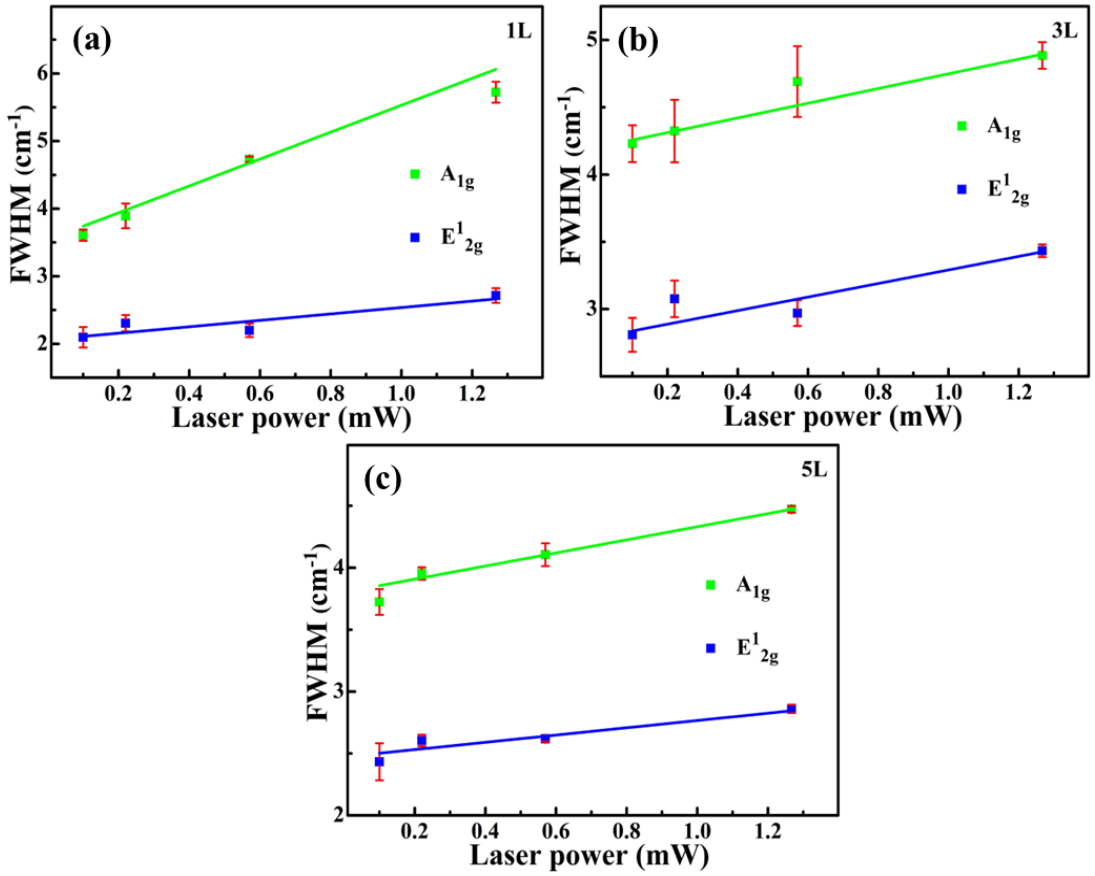

Figure 5.8 *Variations of FWHM for E^1_{2g} and A_{1g} phonon modes with incident laser power for CVD grown triangular (a) 1L, (b) 3L and (c) 5L MoS_2 using 100x objective lens.*

Table 5.2 First order power- and temperature-dependent coefficients for both the E^1_{2g} and A_{1g} phonon modes of supported 1L, 3L and 5L MoS_2.

Layer number of MoS_2	Raman modes	χ_P (cm^{-1} mW^{-1})		χ_T (cm^{-1} K^{-1})
		0.19 μm spot	0.28 μm spot	
1L	E^1_{2g}	1.99 ± 0.67	1.66 ± 0.18	0.0179
	A_{1g}	2.44 ± 0.36	0.98 ± 0.07	0.0112
3L	E^1_{2g}	0.92 ± 0.09	0.84 ± 0.06	0.0143
	A_{1g}	1.61 ± 0.34	0.96 ± 0.19	0.0163
5L	E^1_{2g}	0.68 ± 0.04	0.48 ± 0.08	0.0066
	A_{1g}	1.15 ± 0.21	0.71 ± 0.30	0.0113

Interfacial thermal conductance per unit area (g) and thermal conductivity (k_s) of supported 1L, 3L and 5L MoS_2/SiO_2-Si are evaluated via previously reported optothermal Raman technique using heat diffusion equation in cylindrical coordinates [184, 185]-

$$\frac{1}{r}\frac{d}{dr}\left(r\frac{dT(r)}{dr}\right) - \frac{g}{k_s t}(T(r)-T_{amb}) = -\frac{Q}{k_s} \quad (5.8)$$

where T(r) and T_{amb} are the radial temperature distribution and the global ambient temperature, respectively. While r is the position measured from centre of the laser beam, t is the thickness of the synthesized film and Q is the volumetric optical heating. The above equation is solved using MATLAB simulation [185]. The ratio of thermal resistance (R_m), calculated using two different laser spot size, is a function of g and k_s. Hence to get a unique value of g and k_s, two different values of R_m with two different objective lenses, i.e. 50x LWD and 100x are calculated using following equation-

$$R_m = {\chi_P}/{\alpha\chi_T} \quad (5.9)$$

where α is the optical absorbance coefficient. The values of absorption coefficients (α) are 0.052 and 0.115 for 1L and 2L MoS_2 supported on SiO_2-Si substrate, respectively, as per reported literature [68]. We have calculated the values of α for different layered MoS_2 using following equation-

$$\alpha_{n+1} = \alpha_n + (1-\alpha_n)\alpha_{SL} \quad (5.10)$$

where α_{n+1} and α_n are the absorption coefficient for $(n+1)^{th}$ and n^{th} number of layer and α_{SL} is the absorption coefficient for single layer. The above equation gives $\alpha_3 = 0.161$ and $\alpha_5 = 0.246$. The spot size of the laser for different objective lens is given by [184-187]-

$$r_0 = \frac{\lambda}{\pi \times \text{N.A.}}\, nm \quad (5.11)$$

where λ and N.A. are the wavelength of the incident laser and the numerical aperture of the objective lens, respectively. Thus, for 50x LWD (N.A. = 0.6), r_0 ~0.28×10^{-6} m and for 100x objective lens (N.A. = 0.9), r_0 ~0.19×10^{-6} m, with 532 nm laser. On solving **equation 5.9**

for supported 1L, 3L and 5L triangular MoS_2/SiO_2-Si, we have found two different experimental values of R_m for two different spot size 0.28×10^{-6} m (50x LWD objective lens) and 0.19×10^{-6} m (100x objective lens) and is listed in **Table 5.3**. Then, by solving the MATLAB simulation, we determined the unique value of g and k_s for 1L, 3L and 5L MoS_2 as summarized in **Table 5.3**.

Table 5.3 Absorption coefficient, thermal resistance, interfacial thermal conductance and thermal conductivities of 1L, 3L and 5L MoS_2.

Layer no. of MoS_2	**Absorption coefficient α (%)**	**Thermal resistance R_m (K W^{-1}) (1 x 10^5)**		**Interfacial thermal conductance g (MW m^{-2} K^{-1})**	**Thermal conductivity k_s (W m^{-1} K^{-1})**
		0.19 µm spot	**0.28 µm spot**		
1L	5.2	22.1234	10.8949	(0.97 ± 0.20)	50 ± 2
3L	16.1	6.1380	3.6599	(4.04 ± 0.01)	34 ± 2
5L	24.6	4.1188	2.5429	(6.08 ± 0.17)	28 ± 2

As observed, thermal conductivity of 1L is highest (50 ± 2 W m^{-1} K^{-1}), showing enhanced in-plane thermal transport and this is because of lesser defects in CVD grown film that impacts less phonon defect scattering. As the number of layer increases, the phonon dispersion changes and more and more phase space states become free for Umklapp phonon scattering phenomenon, resulting in the decrease in thermal conductivity [188]. The 'g' value is found to be highest (6.08 ± 0.17 MW m^{-2} K^{-1}) for 5L MoS_2 and lowest (0.97 ± 0.20 MW m^{-2} K^{-1}) for 1L MoS_2, indicating larger heat transfer across interface for few layer MoS_2. The same trend of decrease in thermal conductivity with increasing layer numbers was observed theoretically in earlier report [189]. The comparative analysis of our work on thermal transport properties of MoS_2 using optothermal Raman spectroscopy technique with literature is summarized in **Table 5.4**.

Table 5.4 Thermal conductivity of different MoS_2 films using optothermal Raman technique.

Sample	Preparation Method	Sample Type	Thermal conductivity k_s ($W\ m^{-1}\ K^{-1}$)	References
1L MoS_2 2L MoS_2	Mechanically exfoliated	Suspended Supported Suspended Supported	84 ± 17 55 ± 20 77 ± 25 35 ± 7	ACS Appl. Mater. Interfaces, 2015, **7**, 25923. [68]
Few-layer MoS_2 (11 L)	CVD- grown	Suspended	52	J. Phys. Chem. C, 2013, **117**, 9042. [64]
Few layer MoS_2	Hydrothermal	-	-	Appl. Phys. Lett., 2014, **104**, 081911. [63]
1L MoS_2	Mechanically exfoliated	Supported	-	ACS Appl. Mater. Interfaces, 2014, **6**, 8959. [67]
1L MoS_2 2L MoS_2	Mechanically exfoliated	Supported	-	Nanoscale, 2013, **5**, 9758. [33]
1L MoS_2	Mechanically exfoliated	Supported	62.2	ACS Appl. Mater. Interfaces, 2015, **7**, 5061. [66]
1L MoS_2	Mechanically exfoliated	Suspended	34.5 ± 4	ACS nano, 2014, **8**, 986. [186]
1L MoS_2 2L MoS_2 Multilayer MoS_2	CVD- grown	Suspended	13.3 ± 1.4 15.6 ± 1.5 43.4 ± 9.1	Nanoscale, 2017, **9**, 2541. [190]
5L MoS_2	Mechanically exfoliated	Supported	-	J. Appl. Phys., 2020, **127**, 104301. [191]
1L MoS_2 3L MoS_2 5L MoS_2	CVD- grown	Supported	50 ± 2 34 ± 2 28 ± 2	**Present Work**

Different values of thermal conductivity in previous reports are attributed to the quality of samples, i.e. suspended or supported MoS_2 obtained via exfoliation or CVD techniques. Thermal response of phonons for mechanically exfoliated MoS_2, exhibits almost linear temperature dependency due to the absence of multi-phonon scattering, whereas CVD

synthesized supported films shows higher extent of non-linearity in thermal response of phonons owing to the presence of defects and chemically active sites [192]. Apart from the synthesis technique, thermal conductivity of supported MoS_2 film is usually lower than the suspended film owing to the phonon leakage across the MoS_2 film-substrate interface. The temperature induced Raman shift for supported MoS_2 films strongly depends on the substrate choice and the resulting bond strength between MoS_2 and the substrate. This may also lead to different in-plane strain effects by the substrate, leading to different values of thermal conductivity for supported MoS_2 on different substrates. Also, the interface quality i.e. contamination may affect the interface coupling that resists the phonon transmission and hence, affecting the thermal conductivity [66, 184]. Our CVD grown supported MoS_2 samples show high thermal conductivity compared to other reports on supported films due to the formation of good interface between film and substrate with lesser defects, suggesting high quality of the prepared film. Additionally, the contributions of anharmonicities (thermal expansion, three phonon and four phonon scatterings) in these films with different layer numbers helps to understand thermal transport in MoS_2 based real devices.

5.2.2 Higher Order Phonon Scattering and Thermal Transport Properties of H-MoS_2/SiO_2-Si

The application of MoS_2 in various integrated electronic and optoelectronic devices requires the growth of large-area, high quality and continuous film of MoS_2 over the supportive substrate. So, this section focusses on the thermal analysis of phonon confinement of H-MoS_2/SiO_2-Si. This investigation involves a detailed quantitative examination of the nonlinear temperature-dependent Raman shifts. Then, through a combined approach involving temperature and power-dependent Raman studies, we accurately determined the interfacial thermal conductance (g) and thermal conductivity (k_s) of H-MoS_2/SiO_2-Si, employing the optothermal Raman spectroscopy technique.

5.2.2.1 Characterization of H-MoS_2/SiO_2-Si

The SEM image of the prepared MoS_2 film over SiO_2-Si substrate is depicted in **Figure 2.8 (b)** of **chapter 2**, illustrating the successful growth and formation of a uniform and continuous thin layer of MoS_2. **Figure 2.10 (d)** of **chapter 2** illustrates the AFM image and the corresponding height profile of the grown film, showing film thickness of ~4 nm, suggesting five layers growth. The phase and semiconducting characteristics of the prepared MoS_2 film is validated using Raman and PL spectroscopy, respectively. In the Raman spectrum (**Figure 2.13 (b)** of **chapter 2**), two distinct modes are observed: the E^1_{2g} mode at ~383 cm^{-1}, associated with the in-plane vibration of Mo and S atoms, and the A_{1g} mode at ~407 cm^{-1}, attributed to the out-of-plane vibration of S atoms. The evident ~24 cm^{-1} separation between these two peaks indicating the growth of five layers MoS_2, as suggested in literature [193]. **Figure 2.15 (b)** of **chapter 2** displays the PL spectra showing two prominent peaks at ~674 nm (A-exciton) and ~629 nm (B-exciton) due to excitonic transition from the spin split valence band (VB) to the doubly degenerate conduction band (CB) at K-point of the Brillouin zone (BZ).

5.2.2.2 Temperature-Dependent Raman Study of H-MoS_2/SiO_2-Si

Here, we investigate the temperature-dependent Raman study of H-MoS_2/SiO_2-Si using 50x LWD objective lens. **Figure 5.9 (a, b)** displays the temperature-dependent Raman spectra of the prepared sample in the temperature range of 80 to 193 K and 213 to 333 K, respectively. The Lorentzian fitted Raman spectra exhibit the peak shift with temperature and is observed to show "quasi-linear" behavior with decreasing temperature. To quantify this relationship, a linear approximation (**equation 5.1**) is used and the derive value of χ_T for E^1_{2g} and A_{1g} phonon modes are -0.0106 and -0.0134 $cm^{-1}K^{-1}$, respectively, as shown in **Figure 5.9 (c)**. **Figure 5.9 (d)** illustrates the FWHM of E^1_{2g} and A_{1g} phonon mode within the specified temperature range. The broadening of the phonon mode stems from their decay into two distinct phonons, resulting in a reduction in the lifetime of optical phonons. Further, to understand the observed non-

linearity, we quantitatively analyzed the semi-quantitative model that has an integrating contributions from thermal expansion $(\Delta\omega)_{latt}$ and anharmonic effects $(\Delta\omega)_{anh}$, described through **equations 5.2, 5.3** and **5.6**. The non-linear temperature-dependent Raman response (**equation 5.2**) shows the better fit and the individual contribution of three-phonon, four-phonon and thermal expansion for E^1_{2g} and A_{1g} phonon mode for few-layer MoS_2 are visualized in **Figure 5.9 (e, f)**.

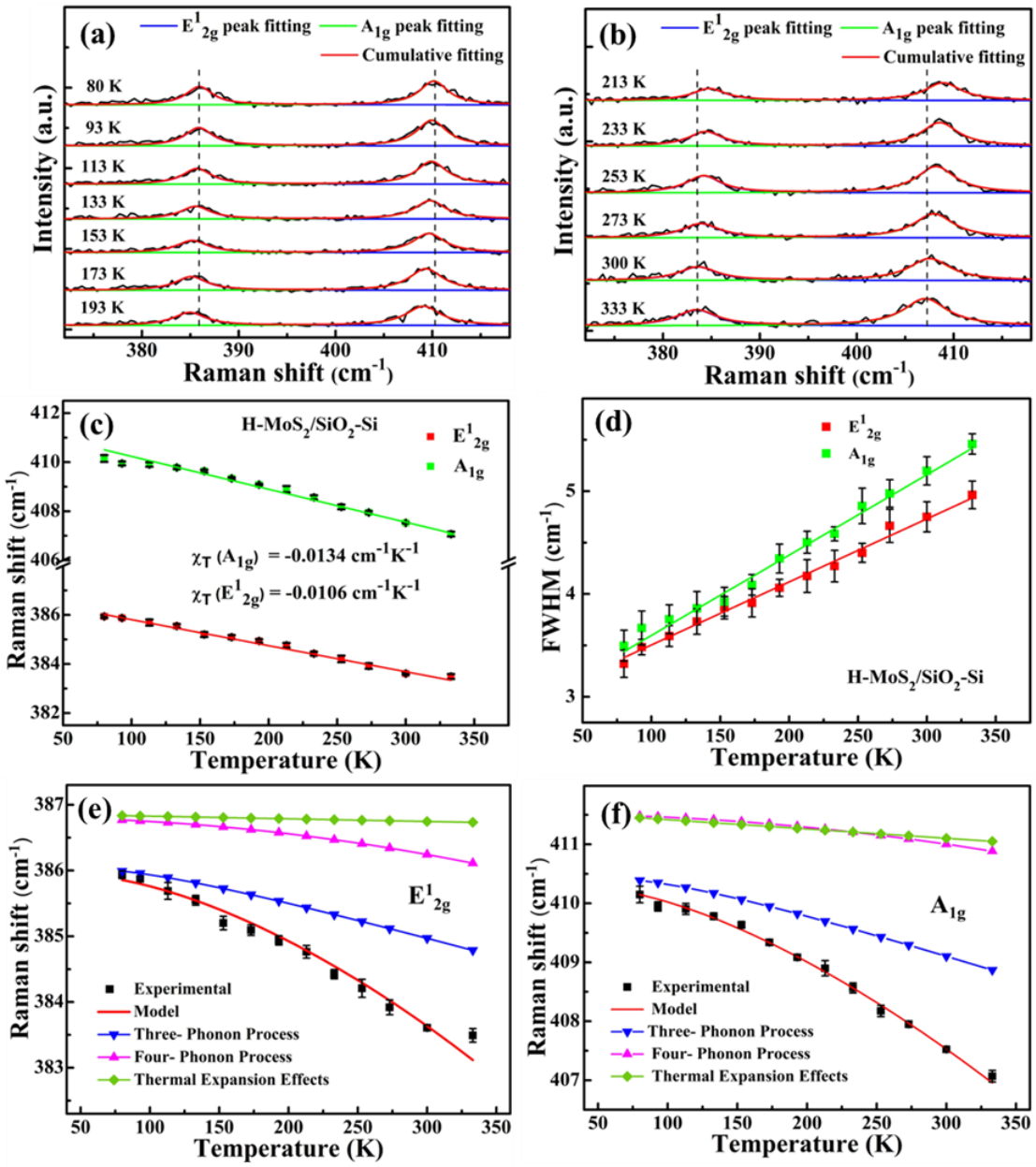

Figure 5.9 *Temperature-dependent Raman spectra from (a) 80 to 193 K and (b) 213 to 333 K of H-MoS_2/SiO_2-Si. Variation in (c) Raman peak positions and (d) FWHM with temperature of H-MoS_2/SiO_2-Si. Individual contributions to three-phonon, four-phonon and thermal expansion in (e) E^1_{2g} and (f) A_{1g} phonon modes of H-MoS_2/SiO_2-Si.*

The obtained values of fitting parameters ω_0 , A and B are 386.87 (411.56), -0.82 (-1.13), -0.07 (-0.07) for E^1_{2g} (A_{1g}) phonon modes, respectively. Our model suggests that the non-linear response observed in both phonon modes predominantly stems from the three-phonon process, with a minimal contribution from the four-phonon process. This finding aligns with expectations as the four-phonon process involves a larger number of phonons and is less probable than the three-phonon process. The observed negligible contribution of thermal expansion for the E^1_{2g} compared to the A_{1g} phonon mode is attributed to a compressive strain at the MoS_2 and SiO_2-Si interface. This strain, caused by the differing thermal expansion coefficients, restricts in-plane expansion compared to out-of-plane expansion, leading to the minimal effect on the E^1_{2g} mode.

5.2.2.3 Calculation for Thermal Conductivity of H-MoS_2/SiO_2-Si

To determine g and k_s of H-MoS_2/SiO_2-Si, we investigated the variation in local temperature of the sample induced by laser heating, as described in previous section. **Figure 5.10 (a, b)** illustrates the room temperature Lorentzian fitted power-dependent Raman spectra, spanning from 0.11 to 1.87 mW, obtained using both 50x LWD and 100x objective lenses, respectively. The observed redshift in both phonon modes with increasing laser power (P) indicates an elevation in the sample's local temperature. **Figure 5.10 (c, d)** depicts the linear correlation between the Raman shift of the E^1_{2g} and A_{1g} phonon modes and increasing laser power, as captured by **equation 5.7**. The calculated values of χ_P for the E^1_{2g} and A_{1g} phonon modes are 0.44 ± 0.05 and 0.74 ± 0.08 $cm^{-1}mW^{-1}$ with the 50x LWD objective lens, and 1.32 ± 0.13 and 1.48 ± 0.13 $cm^{-1}mW^{-1}$ with the 100x objective lens, respectively. Considering the interaction between the MoS_2 film and the substrate, the E^1_{2g} phonon mode displays a comparatively lesser frequency shift. Consequently, we selected the obtained values of the A_{1g} phonon mode to calculate g and k_s. Furthermore, **Figure 5.10 (e, f)** demonstrates the increase in FWHM of both phonon modes under both 50x LWD and 100x objective lenses with

increasing incident laser power. This observed redshift in Raman modes and the rise in FWHM with increased laser power unequivocally indicate lattice expansion and the softening of bonds due to laser-induced heating in the sample.

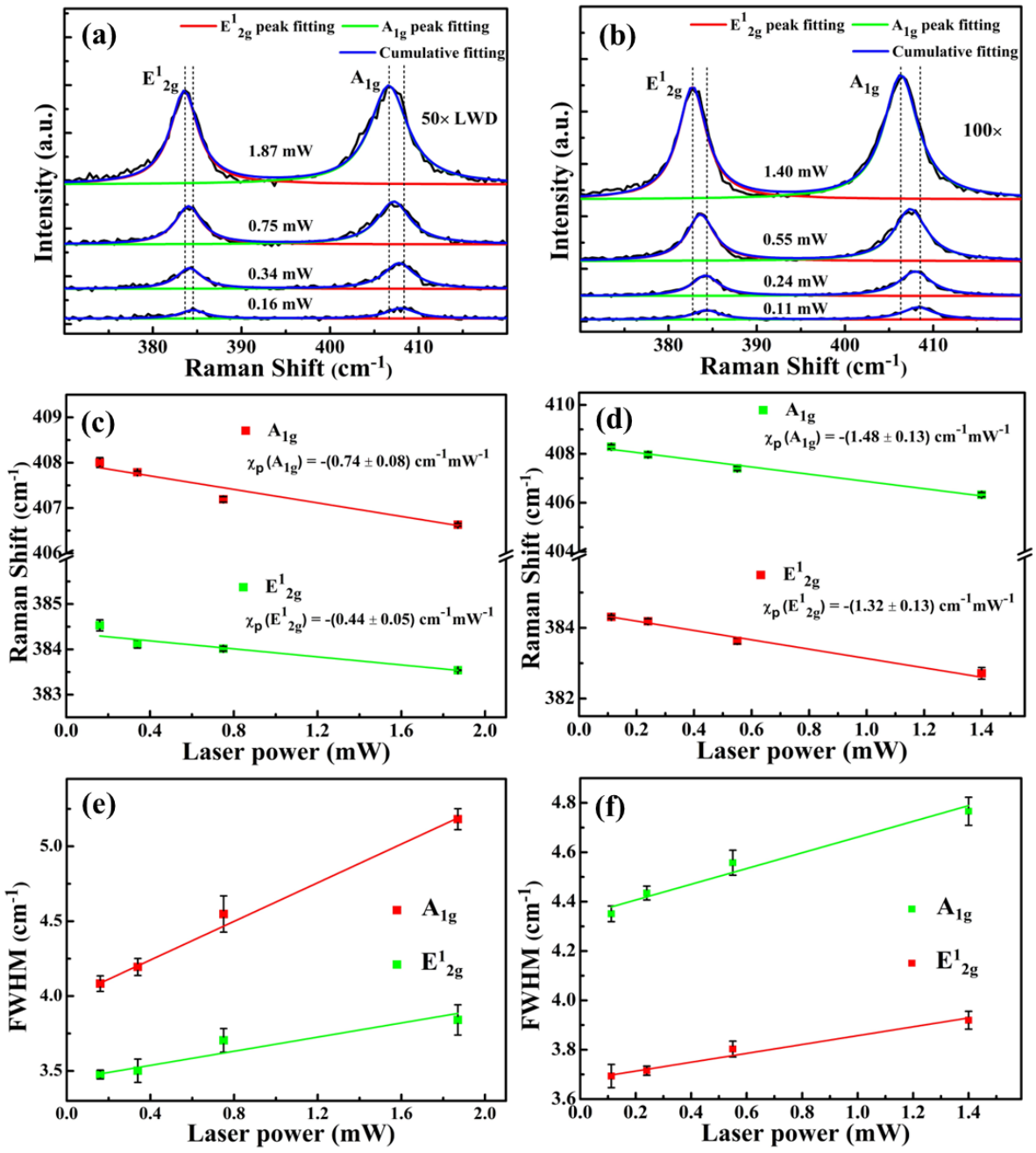

Figure 5.10 *(a, b) Power-dependent Raman spectra, (c, d) variation of peak position with laser power and (e, f) variation of FWHM with laser power for both the phonon modes with 50x LWD and 100x objective lens, respectively on H-MoS_2/SiO_2-Si.*

We determine g and k_s in accordance with the methodology outlined in **section 5.2.1.3**, using MATLAB simulations. For our study, the coefficient α for 5L MoS_2 was calculated using

equation 5.10, yielding α_5 = 0.246. The measured R_m values for the 50x LWD and 100x objective lenses are 2.2449 × 10^5 and 4.4897 × 10^5 KW^{-1}, respectively. Subsequently, employing MATLAB simulations, we determined the values of g and k_s to be ~5.89 ± 0.40 $MWm^{-2}K^{-1}$ and ~33 ± 3 $Wm^{-1}K^{-1}$, correspondingly. Thermal conductivity of suspended materials is largely quenched when supported on a substrate [68, 184]. The H-MoS_2 film is in continuous contact with SiO_2-Si substrate, experiencing maximum strain, that lowers its in-plane thermal conductivity and enhances the interfacial thermal conductance.

5.2.3 Higher Order Phonon Scattering and Thermal Transport Properties of V-MoS_2/SiO_2-Si

In the previous sections, the thermal conductivity of a horizontally grown MoS_2 film on different substrates were discussed. In such configurations, the continuous contact between the horizontally grown MoS_2 film and the substrate produces maximal strain, that led to a decrease in thermal conductivity. Conversely, in vertically oriented MoS_2, the strain is significantly reduced because of the notably smaller contact area between the MoS_2 and the substrate, and thus, in this section we have conducted the similar study for V-MoS_2/SiO_2-Si. Firstly, we explored a comprehensive thermal analysis to investigate the effects of phonon confinement in V-MoS_2/SiO_2-Si. Our approach involves examining the temperature-dependent evolution of phonons and performing a quantitative analysis of the non-linear temperature-dependent Raman shift. Then, we employed the optothermal Raman spectroscopy technique to characterize the thermal properties of these nanostructures accurately. This investigation provides valuable insights into the thermal behavior of these materials, shedding light on their phonon dynamics and thermal transport characteristics. Understanding these properties is pivotal for various applications in nanoelectronics, materials science and thermal management.

5.2.3.1 Characterization of V-MoS_2/SiO_2-Si

The SEM image of V-MoS_2/SiO_2-Si is shown in **Figure 4.15 (a)** of **chapter 4**, indicating the large-scale formation of interconnected and nearly vertical 3D network of MoS_2 nanoflakes. The Raman spectrum of V-MoS_2/SiO_2-Si at room temperature (300 K) is shown in **Figure 5.11 (b)**. The appearance of the in-plane E^1_{2g} and out-of-plane A_{1g} characteristic peaks confirms the presence of the 2H phase of MoS_2. The frequency difference of ~24.6 cm^{-1} between these two peaks suggests the growth of nearly five to six layers MoS_2 and is consistent with previous reports [157].

5.2.3.2 Temperature-Dependent Phonon Study of V-MoS_2/SiO_2-Si

Here, we explore the temperature-dependent Raman study of V-MoS_2/SiO_2-Si. **Figure 5.11 (a, b)** shows the Raman spectra across two temperature ranges: 80 to 193 K and 213 to 333 K, respectively. The Lorentzian fitted Raman spectra reveal noticeable peak shifts, displaying a "quasi-linear" trend with decreasing temperature. For quantitative analysis, we employed a linear approximation (**equation 5.1**), yielding χ_T values of -0.0121 and -0.0169 $cm^{-1}K^{-1}$ for the E^1_{2g} and A_{1g} phonon modes, respectively (**Figure 5.11 (c)**). **Figure 5.11 (d)** depicts the FWHM of E^1_{2g} and A_{1g} phonon modes in the defined temperature range, showing broadening caused by their decay into two separate phonons, leading to a decrease in the lifetime of optical phonons. Additionally, to delve into the observed non-linearity, a quantitative analysis of a semi-quantitative model including contributions from thermal expansion $(\Delta\omega)_{latt}$ and anharmonic effects $(\Delta\omega)_{anh}$ via **equations 5.2, 5.3** and **5.6** was conducted. The non-linear temperature-dependent Raman response (**equation 5.2**) exhibited a superior fit, delineating the individual contributions of three-phonon, four-phonon and thermal expansion effects for the E^1_{2g} and A_{1g} phonon modes in few-layer MoS_2 (**Figure 5.11 (e, f)**).

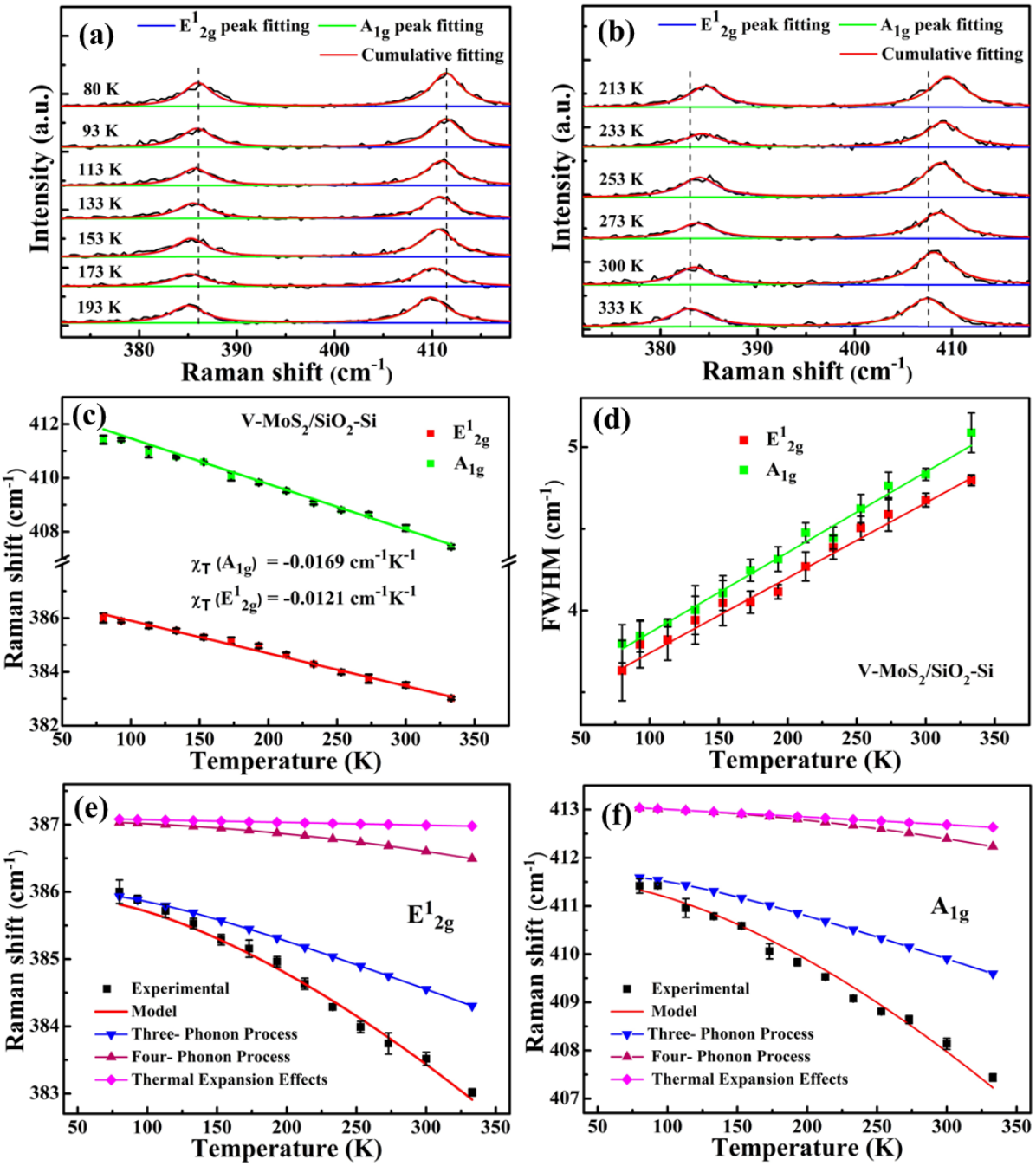

Figure 5.11 *Temperature-dependent Raman spectra from (a) 80 to 193 K and (b) 213 to 333 K of V-MoS_2/SiO_2-Si. Variation in (c) Raman peak positions and (d) FWHM with temperature of V-MoS_2/SiO_2-Si. Individual contributions to three-phonon, four-phonon and thermal expansion in (e) E^1_{2g} and (f) A_{1g} phonon modes of V-MoS_2/SiO_2-Si.*

The fitted parameters ω_0, A and B, were determined as 387.11 (413.16), -1.11 (-1.49), -0.05 (-0.10) for the E^1_{2g} (A_{1g}) phonon modes, respectively. In general, three-phonon scattering process dominates over four phonon process, as observed in our case for both the phonon modes in

prepared MoS_2 films. However, the larger value of B for E^1_{2g} mode of H-MoS_2 (-0.07) compared to V-MoS_2 (-0.05), indicates higher four-phonon contribution for in-plane mode of H-MoS_2 than that of V-MoS_2. This could be due to the large contact area between MoS_2 and substrate in horizontal orientation compared to vertical orientation leading to higher order scattering due to interface formation.

5.2.3.3 Calculation for Thermal Conductivity of V-MoS_2/SiO_2-Si

To assess g and k_s of V-MoS_2/SiO_2-Si, we examine the local temperature variations induced by laser heating as previously detailed. **Figure 5.12 (a, b)** shows room temperature Lorentzian-fitted power-dependent Raman spectra, spanning 0.11-1.87 mW, using 50x LWD and 100x objective lenses, respectively. The observed redshift in both phonon modes with increasing laser power signals indicates the rise of sample's local temperature. **Figure 5.12 (c, d)** describes the linear correlation between Raman shift and laser power, as described by **equation 5.7**. The calculated values of χ_P for the E^1_{2g} and A_{1g} phonon modes are 2.30 ± 0.36 and 2.54 ± 0.51 $cm^{-1}mW^{-1}$ with 50x LWD objective lens, and 2.99 ± 0.18 and 3.49 ± 0.61 $cm^{-1}mW^{-1}$ with 100x objective lens, respectively. The comparatively lesser frequency shift in the E^1_{2g} phonon mode led to the selection of A_{1g} phonon mode values to determine g and k_s. **Figure 5.12 (e, f)** illustrates the increasing FWHM of both phonon modes under both objective lenses as laser power increases. These shifts in Raman modes and FWHM indicates the lattice expansion and bond softening due to laser-induced heating. Proceeding to determine g and k_s as outlined in **section 5.2.1.3**, MATLAB simulations solved the heat diffusion equation (**equation 5.8**) to derive thermal resistance (R_m) as a function of g and k_s. By incorporating α calculated as $\alpha_6 \sim 0.285$ from **equation 5.10**, we obtained the measured R_m values for the 50x LWD and 100x objective lenses to be ~5.27×10^5 and 7.25×10^5 KW^{-1}, respectively. These R_m values using both objective lenses were employed to calculate g and k_s, resulting in values

of ~0.77 ± 0.01 $MWm^{-2}K^{-1}$ and ~62 ± 2 $Wm^{-1}K^{-1}$, respectively. The smaller contact area between V-MoS_2 and SiO_2-Si substrate [194], results in enhanced in-plane thermal conductivity and reduced interfacial thermal conductance.

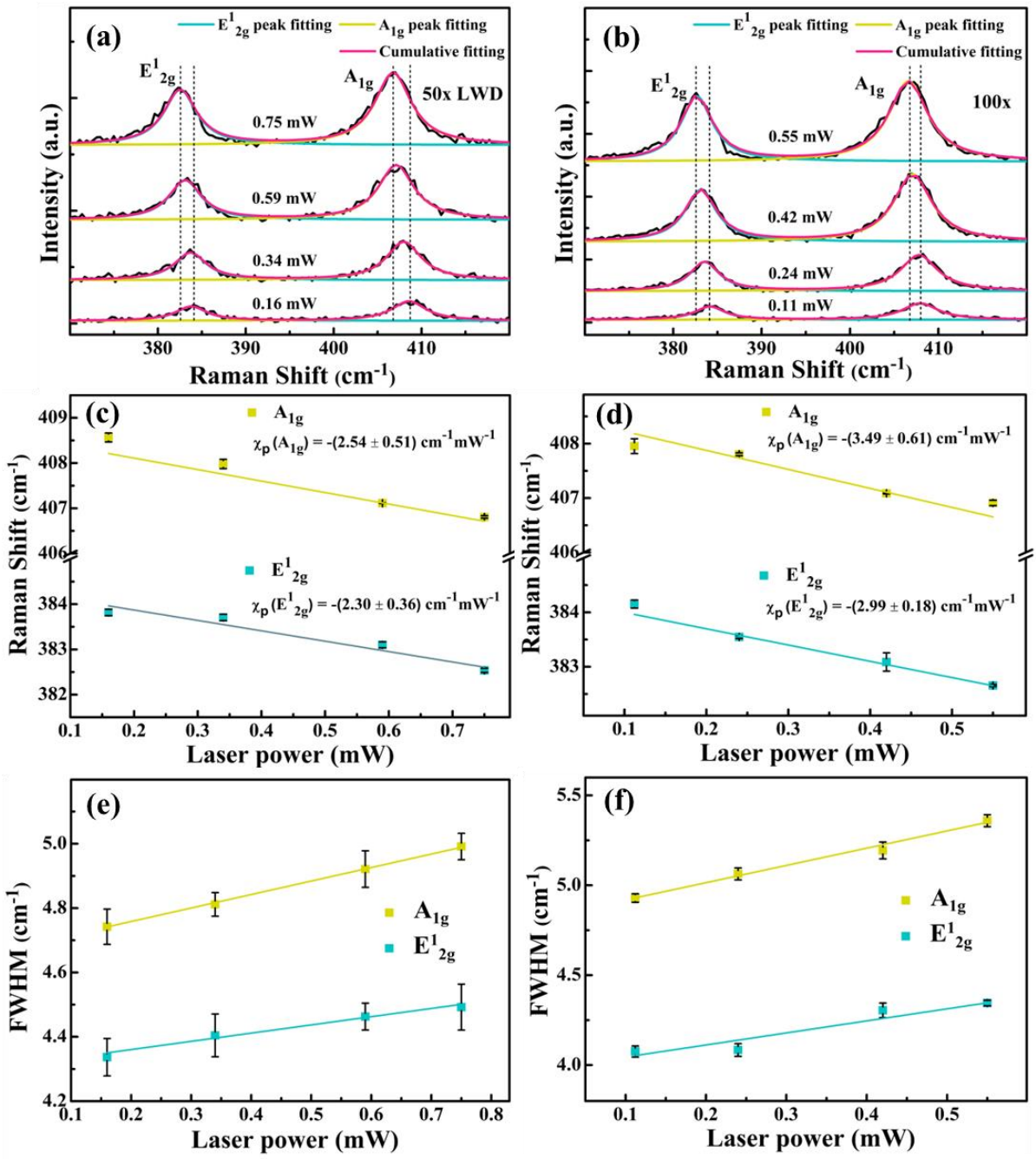

Figure 5.12 *(a, b) Power-dependent Raman spectra, (c, d) variation of peak position with laser power and (e, f) variation of FWHM with laser power for both the phonon modes with 50x LWD and 100x objective lens, respectively on V-MoS_2/SiO_2-Si.*

5.2.4 Higher Order Phonon Scattering and Thermal Transport Properties of H-MoS_2/FTO

In electronic and optoelectronic devices, fluorine-doped tin oxide (FTO) coated glass is used, however, there has not been any report on thermal transport behavior of MoS_2 grown over FTO coated glass. This section touches the higher order phonon scattering and thermal transport properties (interfacial thermal conductance per unit area and thermal conductivity) to advance the understanding of MoS_2 on a common conducting substrate used in applications.

5.2.4.1 Characterization of H-MoS_2/FTO

The SEM image and photograph of grown film over FTO substrate is shown in **Figure 4.22 (a)** of **chapter 4.** The AFM image and height profile of the grown film is shown in **Figure 2.10 (e)** of **chapter 2,** showing film thickness of ~5 nm with surface roughness of 1 nm, suggesting presence of around 7 layers of MoS_2 [19]. The phase and semiconducting nature of the prepared MoS_2 film are confirmed via Raman and photoluminescence (PL) spectroscopy, respectively. The Raman spectrum is shown in **Figure 4.22 (b)** of **chapter 4**. The separation of 25 cm^{-1} between these two prominent peaks (E^1_{2g} mode at ~382 cm^{-1} and A_{1g} mode at ~407 cm^{-1}) suggest the growth of more than six layers, as suggested in literature [19, 168]. **Figure 2.15 (b)** of **chapter 2** shows the two prominent PL peaks at ~673 nm (A-exciton) and ~630 nm (B-exciton) due to excitonic transition from the spin split VB to doubly degenerate CB at K-point of the BZ.

5.2.4.2 Temperature-Dependent Raman Study of H-MoS_2/FTO

We investigate the temperature-dependent Raman study of H-MoS_2/FTO using 50x LWD objective lens. **Figure 5.13 (a, b)** shows the temperature-dependent Raman spectra of the synthesized sample in the temperature range of 80 to 193 K and 213 to 333 K, respectively. The Lorentzian fitted Raman spectra shows the peak shift with temperature for both the phonon modes. The phonon shift with temperature is observed to exhibit “quasi-linear” behavior with

decreasing temperature. So, firstly we analyse the temperature-dependent Raman shift of both the phonon modes using a linear approximation, as described in **equation 5.1**, to obtain χ_T. The linear fitting for the Raman shift of both the phonon modes as a function of temperature is shown in **Figure 5.13 (c)** and the obtained value of χ_T for E^1_{2g} and A_{1g} phonon modes are -0.0136 and -0.0142 $cm^{-1}K^{-1}$, respectively. The FWHM of E^1_{2g} and A_{1g} phonon modes are also systematically studied in this specified temperature range and is shown in **Figure 5.13 (d)**. The decay of both the phonon modes into two different phonons leads to the decrease in the lifetime of optical phonons and produces broadening of phonon modes. Thus, the FWHM of both the phonon modes increases with increasing temperature. Further, we quantitatively analyzed the non-linearity in temperature-dependent Raman response of both the phonon modes from a semi-quantitative model that includes contributions from thermal expansion $(\Delta\omega)_{latt}$ and anharmonic effects $(\Delta\omega)_{anh}$, as described in **equations 5.2, 5.3** and **5.6. Equation 5.2** better fits the non-linear temperature-dependent Raman response and the individual contribution of three-phonon, four-phonon and thermal expansion for E^1_{2g} and A_{1g} phonon mode for few-layer MoS_2 are shown in **Figure 5.13 (e, f)**. The obtained values of fitting parameters ω_0, A and B are 387.48 (412.00), -1.15 (-1.23), -0.09 (-0.08) for E^1_{2g} (A_{1g}) phonon modes, respectively. Our model suggests that the non-linear response of both the phonon modes primarily originates from three-phonon process and a weak contribution from four-phonon process. It is an expected result because four-phonon process involves large number of phonons and so is less likely to occur than the three-phonon process. A compressive strain at the interface of MoS_2 and FTO coated glass, due to the difference in their thermal expansion coefficients, restricts the in-plane expansion compared to out-of-plane expansion and hence, we observe negligible contribution of thermal expansion for E^1_{2g} compared to A_{1g} phonon mode.

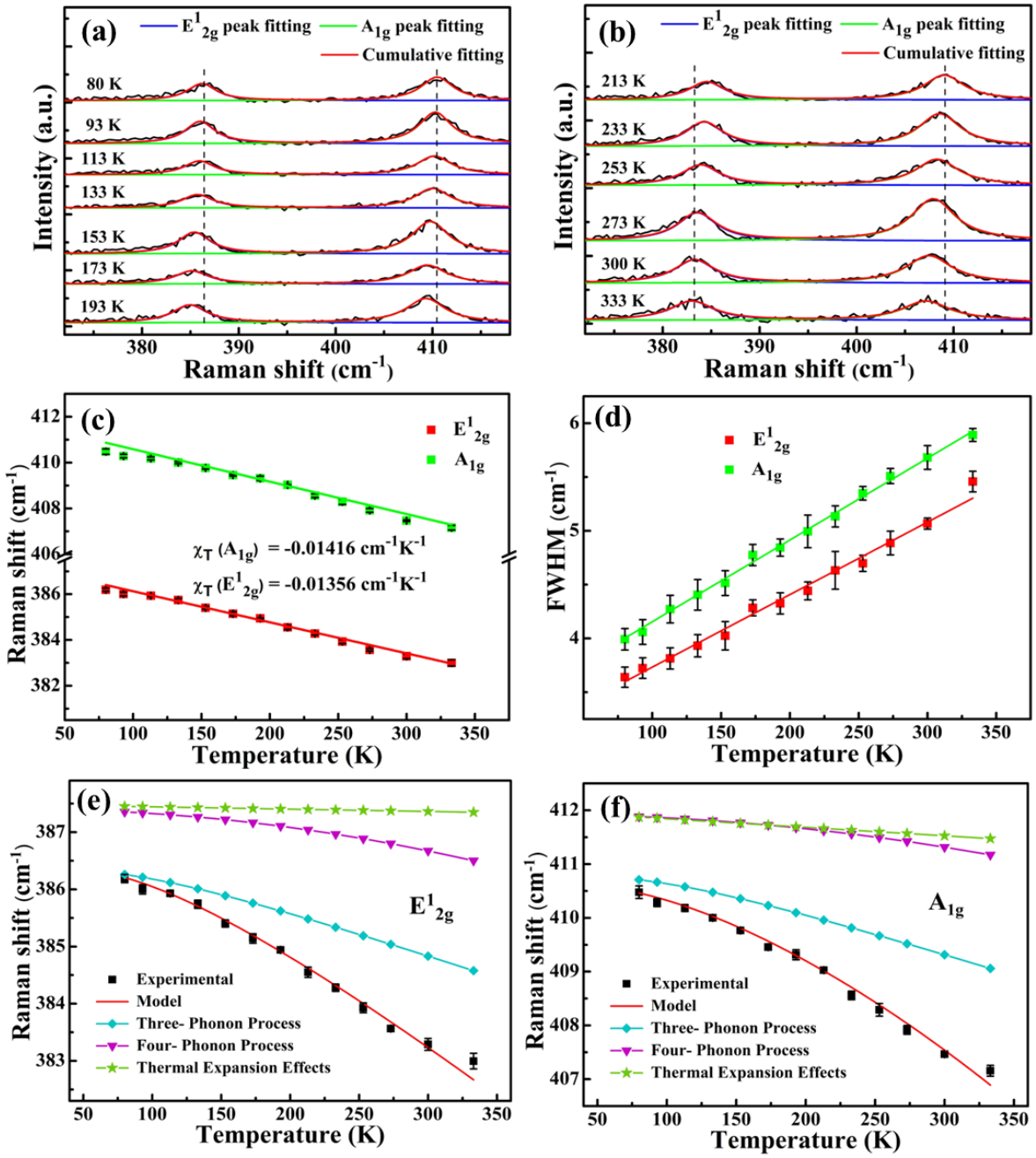

Figure 5.13 *Temperature-dependent Raman spectra from (a) 80 to 193 K and (b) 213 to 333 K of H-MoS_2/FTO. Variation in (c) Raman peak positions and (d) FWHM with temperature of H-MoS_2/FTO. Individual contributions to three-phonon, four-phonon and thermal expansion in (e) E^1_{2g} and (f) A_{1g} phonon modes of H-MoS_2/FTO.*

5.2.4.3 Calculation for Thermal Conductivity of H-MoS_2/FTO

Next, to calculate g and k_s of few-layer MoS_2 supported over FTO coated glass substrate, we observe change in local temperature of the sample due to induced laser heating. **Figure 5.14 (a, b)** shows the room temperature Lorentzian fitted Raman spectra collected at

different laser powers ranging from 0.11 to 1.87 mW, using 50x LWD and 100x objective lenses, respectively. It is observed that as the laser power (P) increases, both the phonon modes are red shifted, indicating the rise in local temperature of the sample. **Figure 5.14 (c, d)** shows the linear dependence of the Raman shift of the two phonon modes (E^1_{2g} and A_{1g}) with increasing laser power under 50x LWD and 100x objective lens, respectively, and can be expressed using **equation 5.7**. The fitted value of χ_P for E^1_{2g} and A_{1g} phonon modes are 0.67 ± 0.07 and 0.83 ± 0.13 $cm^{-1}mW^{-1}$ with 50x LWD objective lens, and 1.22 ± 0.11 and 1.45 ± 0.11 $cm^{-1}mW^{-1}$ with 100x objective lens, respectively. The E^1_{2g} phonon mode exhibits lesser frequency shift owing to the interaction between MoS_2 film and the substrate and thus we choose the obtained values of A_{1g} phonon modes to calculate g and k_s. The FWHM of both the phonon modes, under 50x LWD and 100x objective lens, are observed to increase with increasing incident laser power, as shown in **Figure 5.14 (e, f)**. Thus, the observed redshift of Raman modes and increase in FWHM with increasing laser power clearly indicates that the laser heating in the sample results in lattice expansion and softening of bonds.

Next, we calculate g and k_s as described in **section 5.2.1.3**. We solve the heat diffusion equation (**equation 5.8**) using MATLAB simulation to obtain thermal resistance (R_m) that is a function of g and k_s. We experimentally calculated R_m using two different objective lens 50x LWD and 100x by using **equation 5.9**. Here, α is calculated for 7L MoS_2 using **equation 5.10** and we get $\alpha_7 = 0.3224$. The obtained value of R_m with 50x LWD and 100x are 1.8317×10^5 and 3.2000×10^5 KW^{-1}, respectively. Thus, by solving the MATLAB simulation, we obtain the values of g and k_s to be ~7.22 ± 0.02 $MWm^{-2}K^{-1}$ and ~40 ± 2 $Wm^{-1}K^{-1}$, respectively, for few-layer MoS_2 grown over FTO coated glass substrate. The significant values of g and k_s are owned to the high cross-plane thermal conductivity of underneath conducting FTO substrate (k_s ~10-15 $Wm^{-1}K^{-1}$), as compared to previous reports that commonly used SiO_2-Si substrate (k_s ~1.4 $Wm^{-1}K^{-1}$) [195-197]. Thus, our study shows the high thermal conductivity for CVD

grown few-layer thin film MoS_2 supported over conducting FTO coated glass substrate, making them relevant for electronic and optoelectronic application.

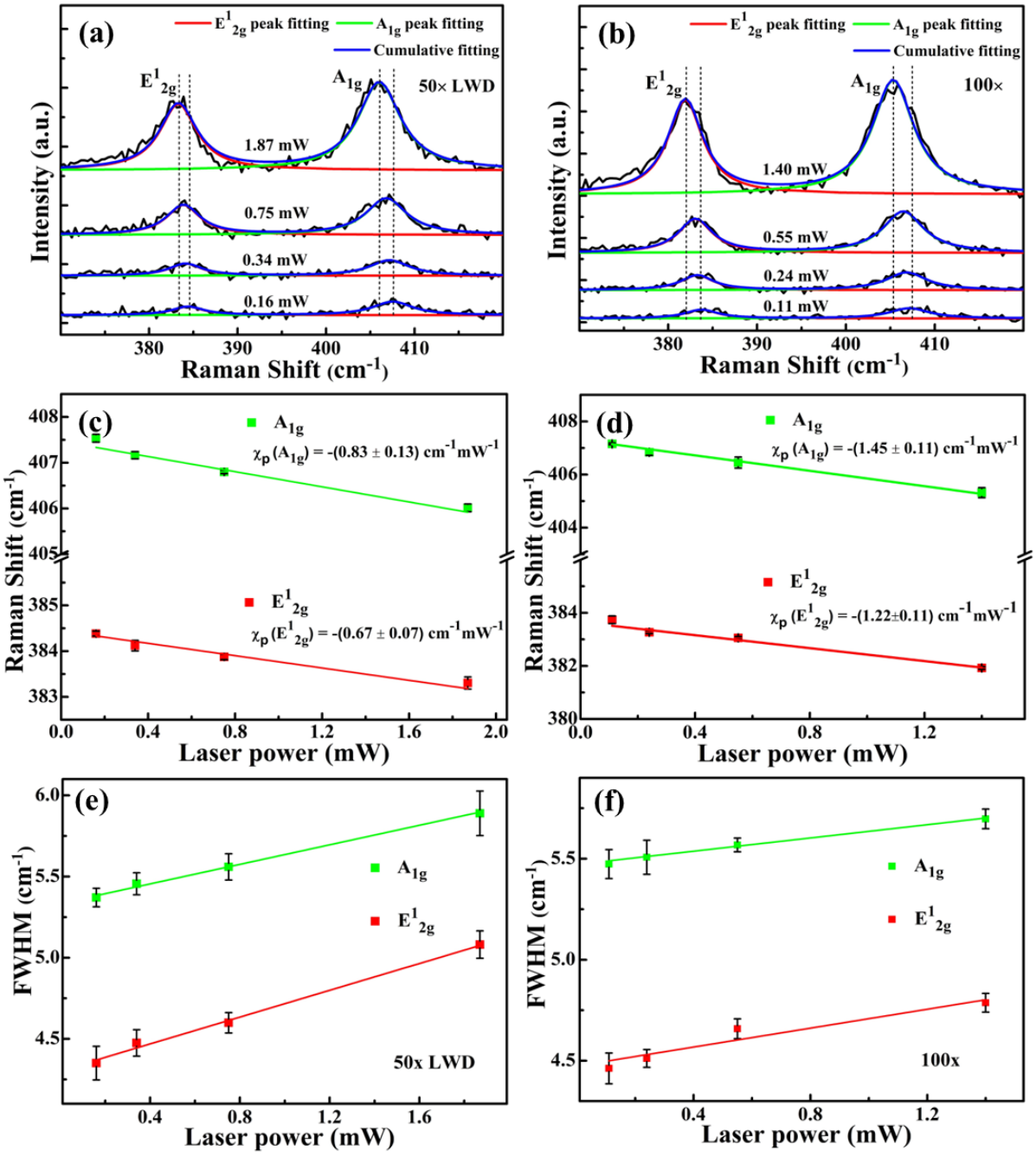

Figure 5.14 *(a, b) Power-dependent Raman spectra, (c, d) variation of peak position with laser power and (e, f) variation of FWHM with laser power for both the phonon modes with 50x LWD and 100x objective lens, respectively.*

5.3 Conclusion

In summary, we scrutinized the thermal transport behavior of different prepared MoS_2 films (1L, 3L and 5L triangular MoS_2/SiO_2-Si, H-MoS_2/SiO_2-Si, V-MoS_2/SiO_2-Si and H-

MoS_2/FTO) using optothermal Raman technique. The systematic understanding of anharmonic behavior was modelled by incorporating both the volume and temperature effects to provide insights into the nonlinear temperature-dependent phonon response, revealing the main non-linearity origin from the three-phonon anharmonic effect in MoS_2. Further, we measured the interfacial thermal conductance (g) and thermal conductivity (k_s) of 1L, 3L and 5L supported MoS_2 and the obtained values of g (k_s) are 0.97 ± 0.20 (50 ± 2), 4.04 ± 0.01 (34 ± 2) and 6.08 ± 0.17 (28 ± 2) W m^{-1} K^{-1}, respectively. The large area interface formation between H-MoS_2 and SiO_2-Si substrate compared to V-MoS_2 leads to higher g in H-MoS_2/SiO_2-Si (~5.89 ± 0.40 $MWm^{-2}K^{-1}$) compared to V-MoS_2/SiO_2-Si (~0.77 ± 0.01 $MWm^{-2}K^{-1}$). The lesser interface formation between V-MoS_2 and SiO_2-Si substrate leads to minimal strain in V-MoS_2 giving it a suspended like characteristics and hence result in higher in-plane thermal conductivity for V-MoS_2 (~62 ± 2 $Wm^{-1}K^{-1}$) compared to H-MoS_2 (~33 ± 3 $Wm^{-1}K^{-1}$). The H-MoS_2/FTO shows higher values of thermal conductivity (k_s ~40 ± 2 $Wm^{-1}K^{-1}$) and interfacial thermal conductance (g ~7.22 ± 0.02 $MWm^{-2}K^{-1}$) compared to H-MoS_2/SiO_2-Si due to the better thermal transport property of FTO in comparison to SiO_2-Si substrate. Our study provides clear insights in MoS_2 nanostructures for designing MoS_2 for better heat management in future applications of low-power thermoelectric and optoelectronic device.